Fermiology of the Dirac type-II semimetal candidates (Ni,Zr)Te_2 using de Haas–van Alphen oscillations

T. Nguyen,[1] N. Aryal,[2,*] Bal K. Pokharel,[3,4] L. Harnagea,[5] D. Mierstchin,[1] Dragana Popović,[3,4] D. E. Graf,[3,4] and K. Shrestha[1,†]

[1]*Department of Chemistry and Physics, West Texas A&M University, Canyon, Texas 79016, USA*
[2]*Condensed Matter Physics and Materials Science Division, Brookhaven National Laboratory, Upton, New York 11973, USA*
[3]*Department of Physics, Florida State University, Tallahassee, Florida 32306, USA*
[4]*National High Magnetic Field Laboratory, Tallahassee, Florida 32310, USA*
[5]*Department of Physics, Indian Institute of Science Education and Research, Pune, Maharashtra 411008, India*

(Received 27 April 2022; revised 8 August 2022; accepted 16 August 2022; published 30 August 2022)

We have investigated the Fermi surface properties of the Dirac type-II semimetal candidates (Ni,Zr)Te_2 using torque magnetometry with applied fields up to 35 T. Magnetization shows clear de Haas–van Alphen (dHvA) oscillations above 20 T. The dHvA oscillations are smooth and well defined and consist of one distinct frequency ($F_\alpha \sim 530$ T) in $ZrTe_2$ and three ($\bar{F}_\alpha \sim 72$ T, $\bar{F}_\beta \sim 425$ T, and $\bar{F}_\gamma \sim 630$ T) in $NiTe_2$. The Berry phase ϕ was determined by constructing the Landau level fan diagram. It is found that $\phi \sim 0$ and π for F_α and $\bar{F}_\beta$, respectively, for $ZrTe_2$ and $NiTe_2$. This strongly suggests that the Dirac fermions make a dominant contribution to the transport properties of $NiTe_2$, whereas topologically trivial fermions dominate those in $ZrTe_2$. The presence of lighter effective mass $m^* = 0.13m_e$ in $NiTe_2$ compared to $m^* = 0.26m_e$ in $ZrTe_2$, where m_e is an electron's rest mass, further confirms the presence of Dirac fermions in $NiTe_2$. Our density functional theory calculations find that while both systems host type-II Dirac dispersions along the out-of-plane direction, their relative positions and the natures of the dispersions are different. The Dirac cone is closer to the Fermi energy E_F (~100 meV above) in $NiTe_2$, whereas it is far (~500 meV) above E_F for $ZrTe_2$. This is consistent with our experimental finding of a nontrivial Berry phase and dominant contribution from lighter electrons in the quantum oscillation signal for only $NiTe_2$. These findings suggest that the proximity of the Dirac cone to E_F in topological compounds is crucial for observing the effect from Dirac quasiparticles in their electrical transport or magnetic properties.

DOI: 10.1103/PhysRevB.106.075154

I. INTRODUCTION

The transition metal dichalcogenides (TMDs; AX_2, $A =$ Mo, W, Ta, Zr, Hf, etc., and $X =$ S, Se, or Te) are interesting as they provide platforms for exploring rich and tunable physical properties, including charge density waves, superconductivity, and magnetism [1–3]. For example, WTe_2 shows extremely large magnetoresistance [4,5], superconductivity was observed in $ZrTe_2$ with intercalation of copper atoms [6], and $TiSe_2$ exhibits a charge density wave [7,8]. Recent studies have shown that TMDs exhibit nontrivial topology, especially Dirac/Weyl type-II properties [9–12], making the study of these materials even more intriguing. In Dirac type-I semimetallic systems, a linearly dispersing Dirac cone exists, whereas the Dirac cone is strongly tilted in type-II semimetals due to the broken Lorenz symmetry [13,14].

Both $ZrTe_2$ and $NiTe_2$ are TMDs, and several reports [15–21] predict that they exhibit the features of massless Dirac fermions. Electronic band structure calculations along with angle-resolved photoemission spectroscopy (ARPES) and quantum oscillation experiments [16–18,22,23] have confirmed the presence of Dirac-like quasiparticles in $NiTe_2$. The Dirac point in $NiTe_2$ is located at ~100 meV above the Fermi level E_F, which is quite a bit closer than in other TMDs, such as $PdTe_2$ (~500 meV) [14], $PtTe_2$ (~800 meV) [13], and $PtSe_2$ (~1200 meV) [24]. Due to the proximity of the Dirac point to E_F in $NiTe_2$, its transport properties might be predominantly derived from Dirac quasiparticles, making it suitable for technological uses [17,18]. In addition, $NiTe_2$ shows pressure-induced superconductivity ($T_c \sim 8$ K) [25], and its monolayer is also predicted to become superconducting ($T_c = 5.7$ K) [26]. Due to the presence of both superconducting and nontrivial topological properties, $NiTe_2$ could be a good candidate for investigating unconventional or possibly topological superconductivity [16]. However, compared to $NiTe_2$, the topological properties of $ZrTe_2$ are not well understood, and the existing reports also do not agree with each other. Theoretical studies predict that $ZrTe_2$ has a simple metallic behavior [27,28], whereas ARPES and nuclear magnetic resonance experiments along with the density functional theory (DFT) calculations [19–21] support a nontrivial topology. Therefore, the topological properties of $ZrTe_2$ have yet to be investigated. To the best of our knowledge, no quantum oscillation studies on $ZrTe_2$ exist, even though it is one of the crucial methods for investigating topological materials [29–33].

---

[*] aryalniraj7@gmail.com
[†] kshrestha@wtamu.edu

In this work, we carry out systematic studies on the Fermi surface and topological features of (Ni,Zr)Te_2 single crystals using the torque magnetometry technique. Both compounds exhibit clear de Haas–van Alphen (dHvA) oscillations with multiple distinct frequencies. Our detailed analyses of dHvA oscillation data show that $ZrTe_2$ is a topologically trivial system, whereas $NiTe_2$ exhibits a nontrivial topology. The angular and temperature dependences of dHvA oscillations are determined to investigate the Fermi surface properties of these materials. The *ab initio* DFT calculations are also presented to support our experimental results.

II. EXPERIMENTAL PROCEDURE

Single crystals of $ZrTe_2$ were grown using the chemical vapor transport technique as described in Refs. [19,34], while those of $NiTe_2$ were synthesized using the self-flux method [35]. The detailed procedures of the material synthesis along with energy dispersive x-ray analyses are presented in the Supplemental Material [36] (Fig. S1). High-field measurements were carried out at the National High Magnetic Field Laboratory (NHMFL), Tallahassee, Florida, with maximum applied fields of 35 T in a dc resistive water-cooled magnet top loaded with a ^{3}He cryostat. Electrical resistance was measured following a standard four-probe method. Platinum wires were attached using silver paint on a freshly cleaved single crystal. A typical contact resistance (Ohmic) at room temperature was 4–5 Ω. The sample was then mounted on the rotating platform of the standard probe designed at NHMFL. An ac current of 1 mA was passed through the sample using a Keithley (6221) source meter. The longitudinal resistance was measured using the lock-in amplifier (SR-830).

Torque magnetization measurements with a miniature piezoresistive cantilever were used to observe dHvA oscillations. A selected sample was fixed to the cantilever arm with vacuum grease, and the arm was then mounted on the rotating platform. The probe then slowly cooled down to the base temperature of 0.32 K. Two resistive elements on the cantilever were incorporated with two room-temperature resistors, forming a Wheatstone bridge, which was balanced at the base temperature before sweeping the magnetic field. The sample was rotated *in situ* with applied fields at different tilt angles θ, where θ is the angle between the magnetic field and the c axis of the sample. Magnetic fields were swept at each fixed temperature at a rate of 2.2 T/min.

Electronic structure calculations were performed on the experimental structures of (Zr,Ni)Te_2 using the QUANTUM ESPRESSO [37] implementation of the DFT in the generalized gradient approximation framework including spin-orbit coupling. The Perdew-Burke-Ernzerhof exchange correlation functional [38] was used with fully relativistic norm-conserving pseudopotentials generated using the optimized norm-conserving Vanderbilt pseudopotentials as described in Ref. [39]. The 4*s*, 4*p*, 4*d*, and 5*s* electrons of Zr and the 4*d*, 5*s*, and 5*p* electrons of Te were treated as valence electrons. The plane-wave energy cutoff was taken to be 80 Ry, and a k-point mesh of $11 \times 11 \times 8$ was used to sample the reducible Brillouin zone (BZ) for the self-consistent calculation. The Fermi surfaces were generated using a more refined k-point mesh of $40 \times 40 \times 30$. The Fermi surface sheets were visualized using the XCRYSDEN software [40]. The angular dependence of the quantum oscillation frequencies was calculated using the SKEAF code [41].

III. EXPERIMENTAL RESULTS AND DISCUSSION

Figures 1(a) and 1(b) display room-temperature x-ray diffraction (XRD) patterns of $ZrTe_2$ and $NiTe_2$ single crystals. All peaks can be indexed with a hexagonal structure [space group $P\bar{3}m1$ (164)], suggesting the presence of a single phase in our samples. In addition, the x-ray diffraction recorded by mounting a single-crystal platelet in Bragg-Brentano geometry showed only peaks with Miller indices (00l) ($l = 1, 2, 3, \ldots$), which implies that the c axis is perpendicular to the plane of the platelet (i.e., the *ab* plane). From x-ray single-crystal diffraction analyses, we obtained the lattice parameters: $a = 3.9457$ Å and $c = 6.6242$ Å for $ZrTe_2$ and $a = 3.8595$ Å and $c = 5.2697$ Å for $NiTe_2$. These lattice parameters are consistent with previous reports [17,42].

Temperature dependences of electrical resistance R for $ZrTe_2$ and $NiTe_2$ are presented in Fig. 1(c). $R(T)$ decreases with decreasing temperature, showing a typical metallic behavior. The residual resistance ratios [$= R(300\text{ K})/R(2\text{ K})$] are estimated to be $\sim$5 and 25 for $ZrTe_2$ and $NiTe_2$, respectively. To understand the magnetotransport properties of these materials, we measured their resistance under high magnetic fields, as shown in Fig. 1(d). Both samples show positive magnetoresistance (MR) with no sign of saturation. The MR of $ZrTe_2$ reaches 100% under 35 T, whereas that of $NiTe_2$ reaches 150% under 14 T. It is important to note that the MR of $ZrTe_2$ shows a parabolic behavior, while that of $NiTe_2$ increases linearly with H. A linear MR in $NiTe_2$ was also observed in an earlier study [17]. In fact, the linear MR is seen in many topological materials [43–45] and is explained as a distinct spectrum of Landau levels for Dirac fermions under magnetic fields. Therefore, the observation of linear MR in $NiTe_2$ here could be due to the dominated transport signal from Dirac electrons. MRs for both materials do not show any sign of Shubnikov–de Haas (SdH) oscillations. So we moved to torque measurements using the piezoresistive cantilever method.

The magnetic torque is given by $\vec{\tau} = V\mu_0\vec{H} \times \vec{M} = V\mu_0 HM \sin\phi$, where V, μ_0, and ϕ represent the volume of the sample, the permeability of the free space, and the angle between M and H, respectively. Assuming $\phi = 90^\circ$, the perpendicular component ($M_\perp$) of the magnetization with the external field can be determined from the torque data. Figures 2(a) and 2(b) represent the $M_\perp$ vs H data for $ZrTe_2$ and $NiTe_2$ single crystals, respectively. Two crystals of each material (Z1 and Z2 from $ZrTe_2$ and N1 and N2 from $NiTe_2$) were used for our experiments. All samples show clear dHvA oscillations at higher fields above 20 T. We subtracted a smooth polynomial background from the dHvA oscillation data and performed the fast Fourier transform (FFT) to determine the frequencies of the oscillations. The frequency spectra of Z1 (N1) and Z2 (N2) have the same number of frequencies, and their values are comparable to one another (see the Supplemental Material [36], Fig. S2).

Figures 2(c) and 2(d) display temperature-dependent FFT spectra for one of the samples for $ZrTe_2$ and $NiTe_2$,

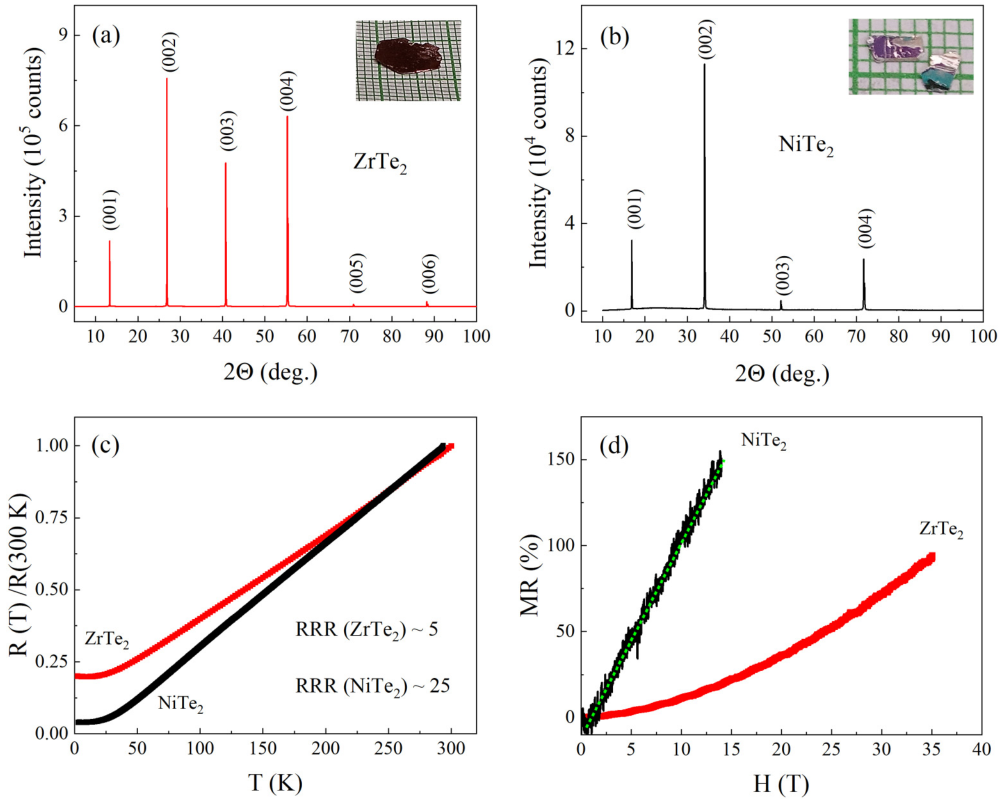

FIG. 1. XRD, electrical resistance, and MR. Room-temperature XRD pattern of (a) $ZrTe_2$ and (b) $NiTe_2$ single crystals indexed in $P\bar{3}m1$ structures. Insets in (a) and (b) show typical single crystals of $ZrTe_2$ and $NiTe_2$, which are $8 \times 8 \times 0.2$ and $3 \times 2 \times 0.3$ mm^3, respectively. (c) R vs T graph for $ZrTe_2$ and $NiTe_2$. $R(T)$ is normalized with the room-temperature value. Resistance for both samples decreases with T, showing a typical metallic behavior. (d) MR of $ZrTe_2$ and $NiTe_2$ samples up to 35 and 14 T, respectively. $NiTe_2$ shows a linear MR, whereas $ZrTe_2$ has a parabolic dependence on the applied field. There is no signature of SdH oscillations in MR for either sample. The dashed line is a guide to an eye.

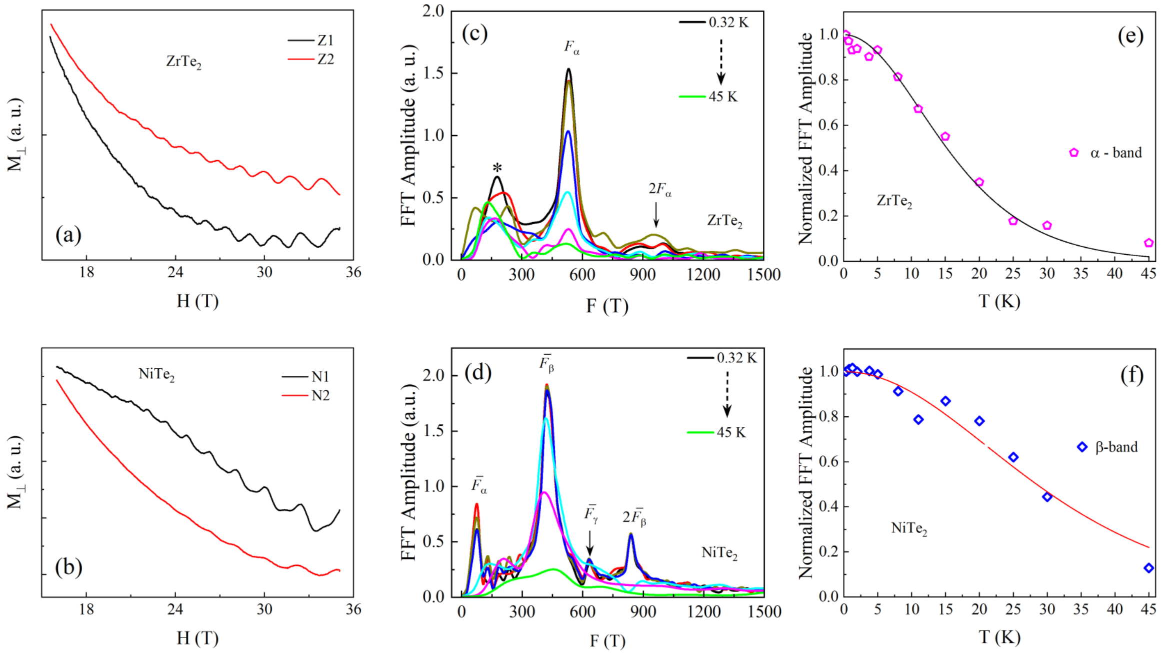

FIG. 2. dHvA oscillations, Fourier transform, and LK fit. Magnetic field dependence of magnetization $M_\perp$ for (a) $ZrTe_2$ (Z1 and Z2) and (b) $NiTe_2$ (N1 and N2) single crystals at $T = 0.32$ K and $\theta = -20^\circ$. $M_\perp$ for both $ZrTe_2$ and $NiTe_2$ show clear dHvA oscillations above 20 T. Temperature-dependent frequency spectra for (c) $ZrTe_2$ (Z1) and (d) $NiTe_2$ (N1). There is one major frequency in $ZrTe_2$, whereas three frequencies are prominent in $NiTe_2$. Lifshitz-Kosevich (LK) analyses for (e) $ZrTe_2$ and (f) $NiTe_2$. Solid curves represent the best-fit curves to the data using the LK formula [Eq. (1)].

respectively. For $ZrTe_2$, a major frequency shows up near $F_\alpha \sim 530$ T. A minor peak appears near 180 T (indicated by an asterisk) which disappears or is not well defined at higher temperatures. Therefore, we do not consider it a major frequency at this moment. Also, a broad peak near 1000 T (nearly $2F_\alpha$) is the second harmonic of F_α. $NiTe_2$ shows three major frequencies at $\bar{F}_\alpha \sim 72$ T, $\bar{F}_\beta \sim 425$ T, and $\bar{F}_\gamma \sim 630$ T. The peak near 840 T is nearly $2\bar{F}_\beta$, so it is the second harmonic of $\bar{F}_\beta$. No quantum oscillation studies on $ZrTe_2$ exist for comparison. However, the frequencies observed in $NiTe_2$ are comparable with those reported by Xu *et al.* [17] and Zheng *et al.* [16]. The frequency F of quantum oscillations is directly proportional to the Fermi wave vector k_F as described by assuming circular extremal orbits in Onsager's relation [29,46] $F = \hbar/(2e)k_F^2$, where $\hbar$ is Planck's constant and k_F is the Fermi wave vector. Therefore, the presence of multiple frequencies in $ZrTe_2$ and $NiTe_2$ implies that there are several Fermi wave vectors corresponding to each frequency, and hence, they have several Fermi surface pockets.

As seen in Figs. 2(c) and 2(d), the FFT amplitude decreases gradually at higher temperatures. This behavior can be explained by the temperature-dependent term in the Lifshitz-Kosevich (LK) formula [46],

$$\Delta\tau(T, H) \propto e^{-\lambda_D} \frac{\lambda(T/H)}{\sinh[\lambda(T/H)]}, \tag{1}$$

with $\lambda_D(H) = \frac{2\pi^2 k_B}{\hbar e} m^* \frac{T_D}{H}$ and $\lambda(T/H) = \frac{2\pi^2 k_B}{\hbar e} m^* \frac{T}{H}$. Here, T_D, k_B, and m^* are the Dingle temperature, Boltzmann's constant, and the effective mass of the charge carriers, respectively. In Eq. [1], the first term represents the attenuation of the oscillations with decreasing field H, whereas the second term describes the weakening of the oscillations at higher temperatures. Due to the presence of multiple frequencies, it is challenging to extract quantum oscillations corresponding to a single frequency from the raw data. For that reason, we have used temperature-dependent FFT data to determine m^* of the charge carriers.

Figures 2(e) and 2(f) show the normalized FFT amplitudes at different temperatures for $ZrTe_2$ and $NiTe_2$, respectively. As can be seen in the graphs, the temperature-dependent FFT data can be explained by the LK formula [Eq. (1)]. Here, we have used the harmonic mean of inverse fields of the FFT interval [32,47,48] while carrying out the LK fit. From the best-fit parameters, we have estimated effective masses to be $m^*_\alpha = (0.26 \pm 0.10)m_o$ for $ZrTe_2$ and $m^*_{\bar{\beta}} = (0.13 \pm 0.11)m_o$ for $NiTe_2$, where m_o is the free-electron mass. Here, $m^*_{\bar{\beta}}$ for $NiTe_2$ is nearly half of the value reported in recent quantum oscillation studies [16,17]. A smaller effective mass of the charge carriers in $NiTe_2$ compared to that in $ZrTe_2$ suggests that the Dirac fermions could be present in $NiTe_2$.

From analyses of dHvA oscillation data, it is clear that multiple Fermi surface pockets exist in both $ZrTe_2$ and $NiTe_2$. To determine the topological nature of these materials, we have calculated the Berry phase ϕ by constructing a Landau level (LL) fan diagram [29,31,46]. Theoretically, ϕ is π for topologically nontrivial systems and zero for trivial systems [29]. Due to the presence of multiple frequencies, it is challenging to separate quantum oscillations corresponding to individual frequencies and then construct a LL fan diagram. Therefore, we have used the bandpass filter to separate the quantum oscillations from the raw data [49–52]. Solid red curves in Fig. 3(a) represent the dHvA oscillations of Z2 (F_α) and N2 ($\bar{F}_\beta$) separated from the raw data (black curves) using bandpass filters of 400–700 and 270–500 T, respectively.

Figure 3(b) shows LL fan plots for $ZrTe_2$ and $NiTe_2$. Here, we have assigned $(n - \frac{1}{4})$ and $(n + \frac{1}{4})$ for the minima and maxima, respectively [49,50], where n represents the LL index. From the linear extrapolation in the limit $1/H \rightarrow 0$ in the LL fan diagram, we have obtained an intercept close to zero for $ZrTe_2$ (-0.02 ± 0.02 for Z1 and -0.12 ± 0.03 for Z2) and 0.5 for $NiTe_2$ (0.42 ± 0.05 for N1 and 0.45 ± 0.05 for N2), which correspond to the ϕ values of ~ 0 and π, respectively. As ϕ is equal to π for a topologically nontrivial system and zero for a trivial system [29,31,33], our Berry phase analyses suggest that $ZrTe_2$ is a trivial system, whereas $NiTe_2$ is nontrivial. In addition, the frequency values (528.6 ± 0.6 T for Z1 and 520.7 ± 1.0 T for Z2 and 402.6 ± 1.4 T for N1 and 400.0 ± 1.4 T for N2) obtained from the linear extrapolation are in good agreement with those in the FFT data (Fig. S3 in the Supplemental Material [36]). This strongly suggests that the bandpass filters still preserve the original signal. As we mentioned earlier, the linear MR in $NiTe_2$ [Fig. 1(d)] and lighter effective mass indicate the presence of Dirac fermions, and this is further confirmed by its nontrivial Berry phase value. Our conclusion of nontrivial topology in $NiTe_2$ is in agreement with other recent quantum oscillation studies [16,17]. However, $ZrTe_2$ shows a trivial Berry phase despite the recent reports [19–21] of its nontrivial topology. To better understand this, we have carried out electronic band structure calculations of both $ZrTe_2$ and $NiTe_2$ using the QUANTUM ESPRESSO [37] implementation of DFT.

IV. DFT CALCULATIONS

A. Band structure and Fermi surface

Figure 4 presents the electronic bands and Fermi surface plots from our DFT calculations for (Zr,Ni)Te_2. As seen in Figs. 4(a) and 4(b), both systems host type-II Dirac dispersion along the Γ-A direction; however, their energy locations and the behaviors of the band dispersion are very different. The existence of the Dirac crossing is guaranteed by the symmetry of the space group in this family of materials. Hence, other members of this family like $PtTe_2$ and $PdTe_2$ also host such dispersion [49]. However, the relative position of the Dirac dispersion from the Fermi level and the nature of the dispersion depend on the electron count, the orbitals involved in the formation of the bands, and other microscopic details of the system.

For the case of $ZrTe_2$, the type-II crossing is $\sim$500 meV from E_F. Moreover, the bands are linear in a very narrow region of k space; hence, it is highly improbable to have any nontrivial observable signals due to such a crossing. The scenario is totally different for the case of $NiTe_2$. Our calculations find the Dirac crossing point to be very close to E_F ($\sim$100 meV above E_F) for $NiTe_2$, and the linear Dirac bands can cross the Fermi level with a very small adjustment. So it is possible to have some nontrivial properties. Note that the exact position of the Dirac crossing depends on the lattice pa-

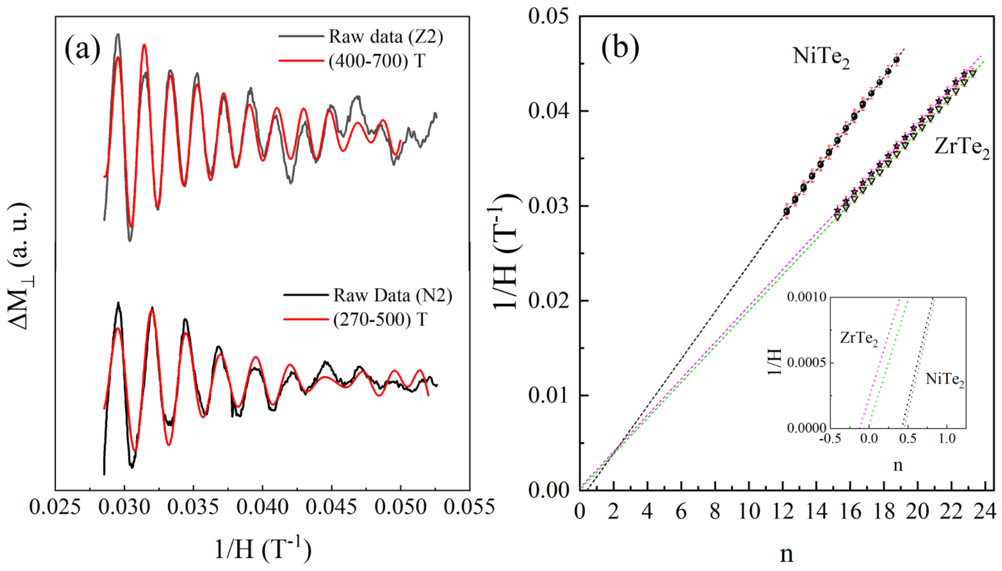

FIG. 3. The bandpass filter and LL fan diagram. (a) The dHvA oscillations for $ZrTe_2$ at $\theta = -20^\circ$ and $NiTe_2$ at $\theta = 20^\circ$. Bandpass filters of 400–700 and 270–500 T are used to select oscillations corresponding to F_α and $\bar{F}_\beta$. The black and red curves represent the raw data and filtered data, respectively. (b) The LL fan diagram for $ZrTe_2$ (F_α) and $NiTe_2$ ($\bar{F}_\beta$). Minima and maxima of the oscillations are assigned to $(n - 1/4)$ and $(n + 1/4)$, respectively, to construct the LL plot. The error bar for each data point is taken as the half-width at half maximum of the respective peak position. The dashed lines are the linear extrapolations of the data. The inset shows the LL plot in the limit $1/\mathrm{H} \to 0$.

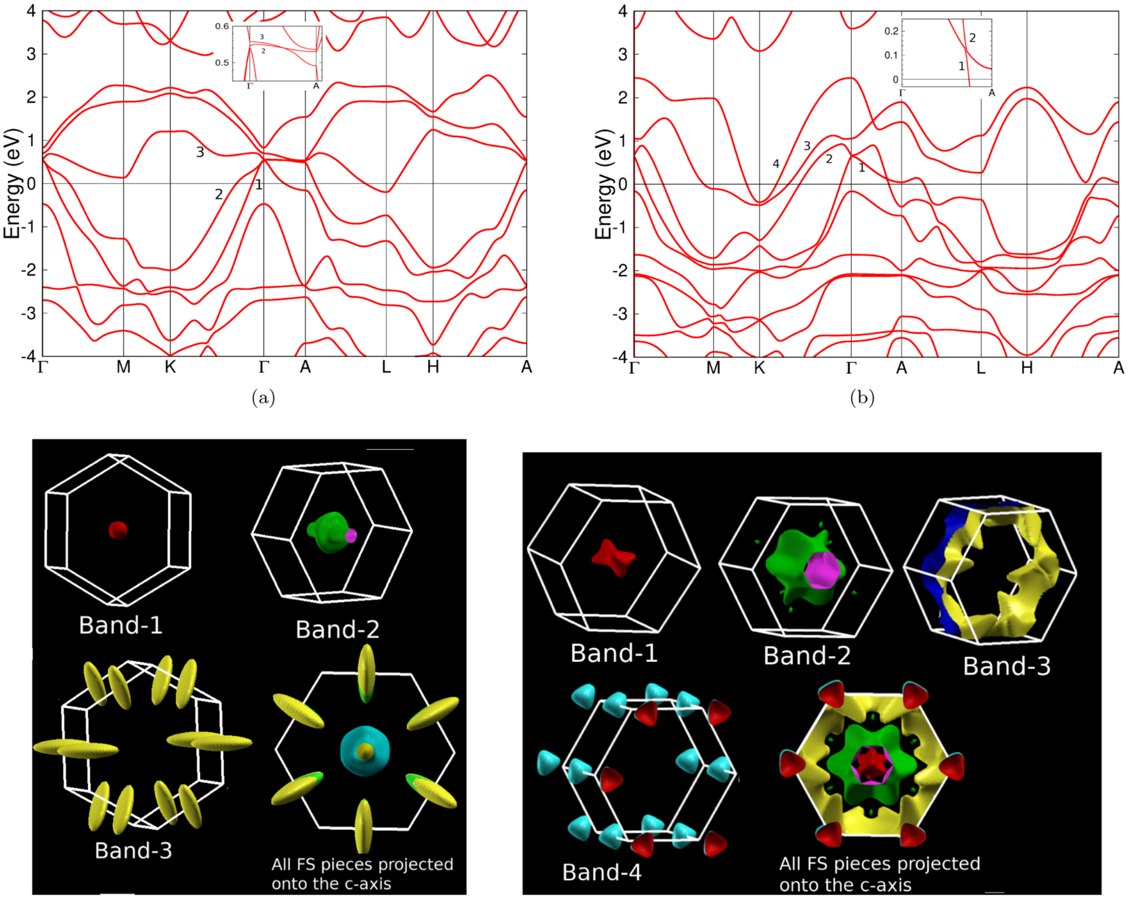

(a) (b)

(c) (d)

FIG. 4. Electronic band structure and Fermi surface. Band structure and Fermi surface of (a) and (c) $ZrTe_2$and (b) and (d) $NiTe_2$ calculated with the inclusion of spin-orbit coupling. The insets in (a) and (b) show zoomed-in bands in a small energy window above the Fermi level to highlight the type-II Dirac crossings along the Γ-*A* direction. In order to identify the bands which cross the Fermi surface, we have labeled the bands based on their energy. See text for details.

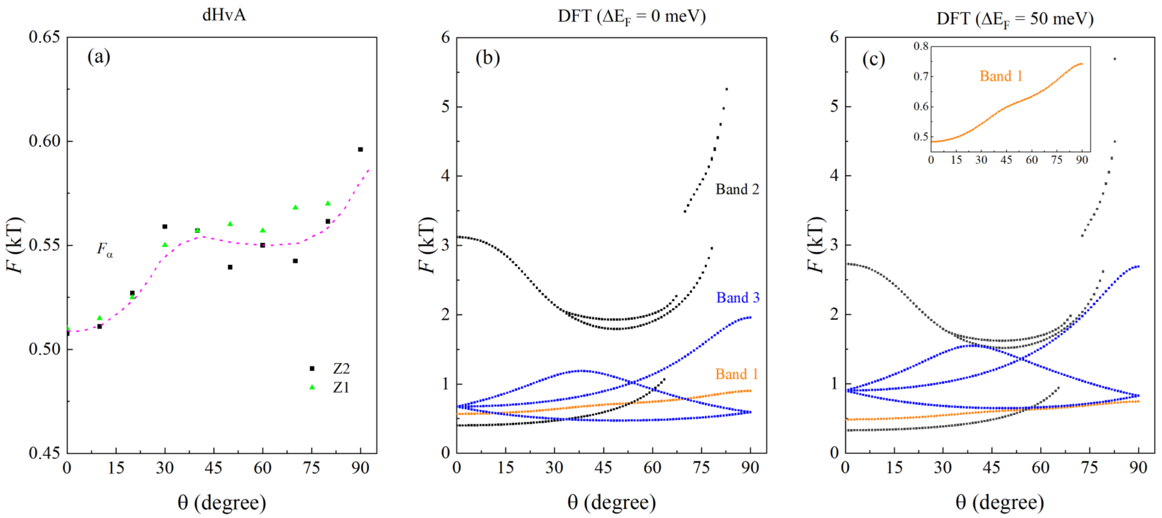

FIG. 5. Frequency vs θ plot. (a) Angular dependence of dHvA oscillation frequencies of $ZrTe_2$ obtained from the torque magnetometry. F_α for Z1 and Z2 are comparable to one another. F_α increases gradually with θ and then decreases after 45°. The dashed curve is a guide to the eye. Calculated Fermi surface frequency for different values of the Fermi levels: (b) $\Delta E_F = 0$ meV and (c) $\Delta E_F = 50$ meV. The inset shows the angular dependence of band 1. F_α (θ) looks qualitatively similar to that of band 1. The frequencies corresponding to bands 2 and 3 do not seem to be present in dHvA oscillations.

rameters and on the different implementations of DFT, which were investigated for $NiTe_2$ in Ref. [16]. The difference of a few tens of meV in the energy position of the Dirac crossing is immaterial for $ZrTe_2$, but it could have some implications in $NiTe_2$ because of its proximity to E_F. More importantly, the linear bands are present only in a very small energy window around E_F. For example, if the Fermi level is very close to the Dirac point such that the bands are still linear, one could expect to get a nontrivial Berry phase associated with the Dirac fermions. However, the absence of the nontrivial Berry phase seen in Ref. [16] could be due to the position of the Fermi level being slightly away from the linear Dirac bands. This could happen for different reasons, e.g., the sample being nonstoichiometric, slight changes in the lattice parameters due to sample growth conditions, etc.

The Fermi surface (FS) plots for (Zr,Ni)Te_2 are shown in Figs. 4(c) and 4(d), respectively. The bands crossing the Fermi level are labeled in the corresponding band structure plots. For the case of $ZrTe_2$, three bands cross E_F; bands 1 and 2 form a holelike FS at the zone center (Γ point), whereas band 3 gives an electronlike FS at the zone boundary around the L high-symmetry point. The shapes of the FS from bands 1 and 3 are elliptical, whereas band 2 forms a "gear-box-like" shape containing the "gear" and the "gear shaft." The FS of $NiTe_2$ looks more complicated than that of $ZrTe_2$ as more bands cross E_F in this case and the FS covers almost the entire Brillouin zone volume. Despite this huge difference, one could still draw some parallels between the two FSs. For example, both crystals have topologically similar Γ-centered hole pockets (bands 1 and 2), with $NiTe_2$ displaying more three-dimensional (3D) FS character, suggesting that the system is strongly bonded along the out-of-plane direction [53]. Also, both systems have electron pockets at the zone boundary, L for $ZrTe_2$ and K for $NiTe_2$. The major difference is the presence of a ringlike electron FS sheet along the zone boundary in $NiTe_2$ which is absent in $ZrTe_2$. This feature is reminiscent of the electron FS feature seen in the sister compounds of $NiTe_2$ such as (Pt,Pd)Te_2.

B. Comparison with the quantum oscillation experiment

In Fig. 5, we present a comparison between the experimental and calculated angular dependences of the calculated FS area for $ZrTe_2$. The Onsager relationship [54] was used to convert the theoretical FS cross-sectional areas into oscillatory frequencies to compare with the experimental values. Here, the value of the angle on the x axis refers to the angle between the crystallographic **c** and the **a** axes, where an angle of 0° corresponds to **H** ∥ **c** axis and 90° corresponds to **H** ∥ **a** axis. Figure 5(a) presents the experimental data, and Fig. 5(b) shows the calculated angular dependence of the Fermi surface when the Fermi level is set to the value obtained from the self-consistent DFT calculation. As seen in these plots, our calculation predicts that there are four distinct frequencies when **H** ∥ **c** axis. Three of the four frequencies are comparable and below 1000 T. They originate from the elliptical pockets at the Γ and L points (bands 1 and 3, respectively) and the Γ-centered cylindrical gear shaft from band 2. However, there is also a large frequency of 3000 T which comes from the gearlike feature from band 2.

We find that in comparison with the experimental angular dependence in Fig. 5(a), there are discrepancies between the experimental and calculated FS areas. The major difference is that the experiment reports just one FS frequency, especially, the higher frequencies (>600 T) which correspond to the electron pocket and the gear hole pocket are missing in the experiment. However, it is not uncommon in quantum oscillation experiments to miss these higher frequencies [55]. By examining the angular dependence of the experimental frequency, it looks like F_α arises from the elliptical pocket of band 1. However, these calculated frequencies are almost twice as large. In order to get a better comparison, we moved the position of the Fermi level upwards. Such movement, although *ad hoc*, corresponds to the doping effect as there is always an ambiguity in the experimental Fermi level. When the Fermi level is shifted upwards, the size of the hole pockets decreases, but that of the electron pockets increases. Such a shift of the Fermi level is, in fact, consistent with the observations of ARPES [19], which shows smaller hole pockets compared to the calculated one. An upwards shift of the Fermi level by ∼50 meV gave a reasonable comparison with the experiment, as seen in Fig. 5(c).

For the angular dependence of $NiTe_2$, we refer the reader to Ref. [16], which involved one of the authors of this work and gives a detailed study and comparison of the calculated FS area with the experimental measurement. The experimental angular dependence presented in this work (see the Supplemental Material [36], Fig. S3) is consistent with the results presented in Ref. [16] with some subtle differences. The reason for this difference could be the weak dependence of the band energies and hence the FS area on the exact position of the Fermi level, which could be different from sample to sample depending on the growth condition and other experimental factors.

V. SUMMARY

In this work, we grew high-quality single crystals of $(Ni,Zr)Te_2$ and studied their electronic properties using the transport, magnetic torque, and *ab initio* DFT calculations methods. The crystallinity and stoichiometry of the samples were confirmed by the XRD and energy dispersive x-ray analysis measurements. The temperature dependences of the resistivity for both $ZrTe_2$ and $NiTe_2$ show good metallic behavior. In order to explore the Fermi surface properties, we carried out MR and magnetic torque measurements under high fields up to 35 T. Neither material shows any sign of quantum oscillations in MR; however, clear and well-defined dHvA oscillations are observed in their magnetization vs H data. There are one major frequency near 530 T for $ZrTe_2$ and three frequencies (72, 425, and 630 T) for $NiTe_2$. The temperature and field dependences of dHvA oscillation data were analyzed using the LK formula, and several physical quantities characterizing the Fermi surface were calculated for both materials. Quite intriguingly, from our Berry phase analyses, we found a trivial topology for $ZrTe_2$ ($\phi \sim 0$) and nontrivial topology for $NiTe_2$ ($\phi \sim \pi$), although both materials were predicted to be Dirac semimetals in recent theoretical and experimental studies. The lighter effective mass and linear magnetoresistance further confirm the presence of Dirac fermions in $NiTe_2$.

For further investigation, we also carried out the electronic band structure and Fermi surfaces calculations using DFT. We found that while both systems host type-II Dirac dispersion along the Γ-A direction, the nature of the Dirac dispersion and its position from the Fermi level are different between the two. The Dirac cone in $NiTe_2$ is closer to E_F (∼100 meV above), as a result of which the Dirac electrons have a dominant effect on transport properties. However, in $ZrTe_2$, the Dirac cone is far from E_F (∼500 meV above); hence, the transport properties are mainly dominated by electrons from the quadratic bands. In addition, the angular dependence of the dHvA oscillation frequencies is consistent with those calculated by the DFT calculations. This work demonstrates that close proximity of the Dirac cone to E_F in topological materials is necessary for Dirac electrons to have a dominant effect on their transport properties and therefore their technological uses.

ACKNOWLEDGMENTS

Work at West Texas A&M University is supported by the Killgore Faculty Research program, the KRC Undergraduate and Graduate Student Research Grants, and the Welch Foundation (Grant No. AE-0025). L.H. acknowledges the Department of Science and Technology (DST), India [Grant No. SR/WOS-A/PM-33/2018(G)]. A portion of this work was performed at the National High Magnetic Field Laboratory, which is supported by National Science Foundation Cooperative Agreement No. DMR-1644779 and the state of Florida. The work by B.K.P. and D.P. was also supported by NSF Grant No. DMR-1707785.

---

[1] S. Manzeli, D. Ovchinnikov, D. Pasquier, O. V. Yazyev, and A. Kis, 2D transition metal dichalcogenides, Nat. Rev. Mater. **2**, 17033 (2017).

[2] Y. I. Joe, X. M. Chen, P. Ghaemi, K. D. Finkelstein, G. A. de la Peña, Y. Gan, J. C. T. Lee, S. Y. amd J. Geck, T. C. C. G. J. MacDougall, S. L. Cooper, E. Fradkin, and P. Abbamonte, Emergence of charge density wave domain walls above the superconducting dome in 1t-$TiSe_2$, Nat. Phys. **10**, 421 (2014).

[3] X. Zhu, Y. Guo, H. Cheng, J. Dai, X. An, J. Zhao, K. Tian, S. Wei, X. C. Zeng, C. Wu, and Y. Xie, Signature of coexistence of superconductivity and ferromagnetism in two-dimensional $NbSe_2$ triggered by surface molecular adsorption, Nat. Commun. **7**, 11210 (2016).

[4] M. N. Ali, J. Xiong, S. Flynn, J. Tao, Q. D. Gibson, L. M. Schoop, T. Liang, N. Haldolaarachchige, M. Hirschberger, N. P. Ong, and R. J. Cava, Large, non-saturating magnetoresistance in WTe_2, Nature (London) **514**, 205 (2014).

[5] Y. Wu, N. H. Jo, D. Mou, L. Huang, S. L. Bud'ko, P. C. Canfield, and A. Kaminski, Three-dimensionality of the bulk electronic structure in WTe_2, Phys. Rev. B **95**, 195138 (2017).

[6] A. J. S. Machado, N. P. Baptista, B. S. de Lima, N. Chaia, T. W. Grant, L. E. Corrêa, S. T. Renosto, A. C. Scaramussa, R. F. Jardim, M. S. Torikachvili, J. A. Aguiar, O. C. Cigarroa, L. T. F. Eleno, and Z. Fisk, Evidence for topological behavior in superconducting Cu_xZrTe_{2-y}, Phys. Rev. B **95**, 144505 (2017).

[7] T. E. Kidd, T. Miller, M. Y. Chou, and T.-C. Chiang, Electron-Hole Coupling and the Charge Density Wave Transition in $TiSe_2$, Phys. Rev. Lett. **88**, 226402 (2002).

[8] M. Porer, U. Leierseder, J.-M. Ménard, H. Dachraoui, L. Mouchliadis, I. E. Perakis, U. Heinzmann, J. Demsar, K. Rossnagel, and R. Huber, Non-thermal separation of electronic

and structural orders in a persisting charge density wave, Nat. Mater. **13**, 857 (2014).

[9] I. Belopolski *et al.*, Fermi arc electronic structure and Chern numbers in the type-II Weyl semimetal candidate $Mo_xW_{1-x}Te_2$, Phys. Rev. B **94**, 085127 (2016).

[10] M. S. Bahramy *et al.*, Ubiquitous formation of bulk Dirac cones and topological surface states from a single orbital manifold in transition-metal dichalcogenides, Nat. Mater. **17**, 21 (2018).

[11] F. Fei, X. Bo, R. Wang, B. Wu, J. Jiang, D. Fu, M. Gao, H. Zheng, Y. Chen, X. Wang, H. Bu, F. Song, X. Wan, B. Wang, and G. Wang, Nontrivial Berry phase and type-II Dirac transport in the layered material $PdTe_2$, Phys. Rev. B **96**, 041201(R) (2017).

[12] R. C. Xiao, P. L. Gong, Q. S. Wu, W. J. Lu, M. J. Wei, J. Y. Li, H. Y. Lv, X. Luo, P. Tong, X. B. Zhu, and Y. P. Sun, Manipulation of type-I and type-II Dirac points in $PdTe_2$ superconductor by external pressure, Phys. Rev. B **96**, 075101 (2017).

[13] M. Yan, H. Huang, K. Zhang, E. Wang, W. Yao, K. Deng, G. Wan, H. Zhang, M. Arita, H. Yang, Z. Sun, H. Yao, Y. Wu, S. Fan, W. Duan, and S. Zhou, Lorentz-violating type-II dirac fermions in transition metal dichalcogenide $PtTe_2$, Nat. Commun. **8**, 257 (2017).

[14] H.-J. Noh, J. Jeong, E.-J. Cho, K. Kim, B. I. Min, and B.-G. Park, Experimental Realization of Type-II Dirac Fermions in a $PdTe_2$ Superconductor, Phys. Rev. Lett. **119**, 016401 (2017).

[15] P. P. Ferreira, A. L. R. Manesco, T. T. Dorini, L. E. Correa, G. Weber, A. J. S. Machado, and L. T. F. Eleno, Strain engineering the topological type-II Dirac semimetal $NiTe_2$, Phys. Rev. B **103**, 125134 (2021).

[16] W. Zheng, R. Schönemann, S. Mozaffari, Y.-C. Chiu, Z. B. Goraum, N. Aryal, E. Manousakis, T. M. Siegrist, K. Wei, and L. Balicas, Bulk Fermi surfaces of the Dirac type-II semimetallic candidate $NiTe_2$, Phys. Rev. B **102**, 125103 (2020).

[17] C. Xu, B. Li, W. Jiao, W. Zhou, B. Qian, R. Sankar, N. D. Zhigadlo, Y. Qi, D. Qian, F.-C. Chou, and X. Xu, Topological type-II Dirac fermions approaching the Fermi level in a transition metal dichalcogenide $NiTe_2$, Chem. Mater. **30**, 4823 (2018).

[18] B. Ghosh, D. Mondal, C.-N. Kuo, C. S. Lue, J. Nayak, J. Fujii, I. Vobornik, A. Politano, and A. Agarwal, Observation of bulk states and spin-polarized topological surface states in transition metal dichalcogenide Dirac semimetal candidate $NiTe_2$, Phys. Rev. B **100**, 195134 (2019).

[19] I. Kar, J. Chatterjee, L. Harnagea, Y. Kushnirenko, A. V. Fedorov, D. Shrivastava, B. Büchner, P. Mahadevan, and S. Thirupathaiah, Metal-chalcogen bond-length induced electronic phase transition from semiconductor to topological semimetal in ZrX_2 (X=Se and Te), Phys. Rev. B **101**, 165122 (2020).

[20] P. Tsipas, D. Tsoutsou, S. Fragkos, R. Sant, C. Alvarez, H. Okuno, G. Renaud, R. Alcotte, T. Baron, and A. Dimoulas, Massless Dirac fermions in $ZrTe_2$ semimetal grown on InAs(111) by van der Waals epitaxy, ACS Nano **12**, 1696 (2018).

[21] Y. Tian, N. Ghassemi, and J. J. H. Ross, Topological nodal line in $ZrTe_2$ demonstrated by nuclear magnetic resonance, Phys. Rev. B **102**, 165149 (2020).

[22] S. Mukherjee, S. W. Jung, S. F. Weber, C. Xu, D. Qian, X. Xu, P. K. Biswas, T. K. Kim, L. C. Chapon, M. D. Watson, J. B. Neaton, and C. Cacho, Fermi-crossing type-II Dirac fermions and topological surface states in $NiTe_2$, Sci. Rep. **10**, 12957 (2020).

[23] J. Zhang and G. Q. Huang, The superconductivity and topological surface state of type-II Dirac semimetal $NiTe_2$, J. Phys.: Condens. Matter **32**, 205702 (2020).

[24] H. Huang, S. Zhou, and W. Duan, Type-II Dirac fermions in the $PtSe_2$ class of transition metal dichalcogenides, Phys. Rev. B **94**, 121117(R) (2016).

[25] Z. Feng *et al.*, Evidences for pressure-induced two-phase superconductivity and mixed structures of $NiTe_2$ and NiTe in type-II Dirac semimetal $NiTe_{2-x}$ ($x = 0.38 \pm 0.09$) single crystals, Mater. Today **17**, 100339 (2021).

[26] F. Zheng, X.-B. Li, P. Tan, Y. Lin, L. Xiong, X. Chen, and J. Feng, Emergent superconductivity in two-dimensional $NiTe_2$ crystals, Phys. Rev. B **101**, 100505(R) (2020).

[27] A. H. Reshak and S. Auluck, Theoretical investigation of the electronic and optical properties of ZrX_2 (X = S, Se and Te), Phys. B (Amsterdam, Neth.) **353**, 230 (2004).

[28] A. Kumar, H. He, R. Pandey, P. K. Ahluwalia, and K. Tankeshwar, Pressure and electric field-induced metallization in the phase-engineered ZrX_2 (X = S, Se, Te) bilayers, Phys. Chem. Chem. Phys. **17**, 19215 (2015).

[29] K. Shrestha, V. Marinova, D. Graf, B. Lorenz, and C. W. Chu, Quantum oscillations in metallic Sb_2Te_2Se topological insulator, Phys. Rev. B **95**, 075102 (2017).

[30] K. Shrestha, V. Marinova, B. Lorenz, and P. C. W. Chu, Shubnikov–de Haas oscillations from topological surface states of metallic $Bi_2Se_{2.1}Te_{0.9}$, Phys. Rev. B **90**, 241111(R) (2014).

[31] K. Shrestha, D. E. Graf, V. Marinova, B. Lorenz, and P. C. W. Chu, Simultaneous detection of quantum oscillations from bulk and topological surface states in metallic $Bi_2Se_{2.1}Te_{0.9}$, Philos. Mag. **97**, 1740 (2017).

[32] K. Shrestha, V. Marinova, D. Graf, B. Lorenz, and C. W. Chu, Large magnetoresistance and Fermi surface study of Sb_2Se_2Te single crystal, J. Appl. Phys. **122**, 125901 (2017).

[33] K. Shrestha, V. Marinova, B. Lorenz, and C. W. Chu, Evidence of a 2D Fermi surface due to surface states in a p-type metallic Bi_2Te_3, J. Phys.: Condens. Matter **30**, 185601 (2018).

[34] N. Pistawala, D. Rout, K. Saurabh, R. Bag, K. Karmakar, L. Harnagea, and S. Singh, Crystal growth of quantum materials: A review of selective materials and techniques, Bull. Mater. Sci. **45**, 10 (2022).

[35] I. Kar, L. Harnagea, S. Banik, S. Singh, and S. Thirupathaiah, Observation of surface Dirac state in transition metal dichalcogenide $NiTe_2$ using ARPES, in *DAE Solid State Physics Symposium 2019*, AIP Conf. Proc. No. 2265 (AIP, Melville, NY, 2020), p. 030361.

[36] See Supplemental Material at http://link.aps.org/supplemental/10.1103/PhysRevB.106.075154 for detailed information on the sample synthesis, energy dispersive x-ray analyses, angle-dependent frequency data, etc.

[37] P. Giannozzi *et al.*, Quantum Espresso: A modular and open-source software project for quantum simulations of materials, J. Phys.: Condens. Matter **21**, 395502 (2009).

[38] J. P. Perdew, K. Burke, and M. Ernzerhof, Generalized Gradient Approximation Made Simple, Phys. Rev. Lett. **77**, 3865 (1996).

[39] D. R. Hamann, Optimized norm-conserving Vanderbilt pseudopotentials, Phys. Rev. B **88**, 085117 (2013).

[40] A. Kokalj, XCrysden—A new program for displaying crystalline structures and electron densities, J. Mol. Graphics Modell. **17**, 176 (1999).

[41] P. Rourke and S. Julian, Numerical extraction of de Haas–van Alphen frequencies from calculated band energies, Comput. Phys. Commun. **183**, 324 (2012).

[42] Y. Wang, C. Xie, J. Li, Z. Du, L. Cao, Y. Han, L. Zu, H. Zhang, H. Zhu, X. Zhang, Y. Xiong, and W. Zhao, Weak Kondo effect in the monocrystalline transition metal dichalcogenide $ZrTe_2$, Phys. Rev. B **103**, 174418 (2021).

[43] A. A. Abrikosov, Quantum magnetoresistance, Phys. Rev. B **58**, 2788 (1998).

[44] X. Z. Xing, C. Q. Xu, N. Zhou, B. Li, J. Zhang, Z. X. Shi, and X. Xu, Large linear magnetoresistance in a transition-metal stannide β-$RhSn_4$, Appl. Phys. Lett. **109**, 122403 (2016).

[45] T. Liang, Q. Gibson, M. N. Ali, M. Liu, R. J. Cava, and N. P. Ong, Ultrahigh mobility and giant magnetoresistance in the Dirac semimetal Cd_3As_2, Nat. Mater. **14**, 280 (2015).

[46] D. Shoenberg, *Magnetic Oscillations in Metals* (Cambridge University Press, Cambridge, 1984).

[47] Y. Fu, N. Zhao, Z. Chen, Q. Yin, Z. Tu, C. Gong, C. Xi, X. Zhu, Y. Sun, K. Liu, and H. Lei, Quantum Transport Evidence of Topological Band Structures of Kagome Superconductor CsV_3Sb_5, Phys. Rev. Lett. **127**, 207002 (2021).

[48] D. Rhodes, S. Das, Q. R. Zhang, B. Zeng, N. R. Pradhan, N. Kikugawa, E. Manousakis, and L. Balicas, Role of spin-orbit coupling and evolution of the electronic structure of WTe_2 under an external magnetic field, Phys. Rev. B **92**, 125152 (2015).

[49] W. Zheng, R. Schönemann, N. Aryal, Q. Zhou, D. Rhodes, Y.-C. Chiu, K.-W. Chen, E. Kampert, T. Förster, T. J. Martin, G. T. McCandless, J. Y. Chan, E. Manousakis, and L. Balicas, Detailed study of the Fermi surfaces of the type-II Dirac semimetallic candidates XTe_2 (X = Pd, Pt), Phys. Rev. B **97**, 235154 (2018).

[50] K. Shrestha, R. Chapai, Bal K. Pokharel, D. Miertschin, T. Nguyen, X. Zhou, D. Y. Chung, M. G. Kanatzidis, J. F. Mitchell, U. Welp, Dragana Popović, D. E. Graf, B. Lorenz, and W. K. Kwok, Nontrivial Fermi surface topology of the kagome superconductor CsV_3Sb_5 probed by de Haas–van Alphen oscillations, Phys. Rev. B **105**, 024508 (2022).

[51] M. A. Khan, D. E. Graf, I. Vekhter, D. A. Browne, J. F. DiTusa, W. A. Phelan, and D. P. Young, Quantum oscillations and a nontrivial Berry phase in the noncentrosymmetric topological superconductor candidate BiPd, Phys. Rev. B **99**, 020507(R) (2019).

[52] R. Chapai, D. A. Browne, D. E. Graf, J. F. DiTusa, and R. Jin, Quantum oscillations with angular dependence in $PdTe_2$ single crystals, J. Phys.: Condens. Matter **33**, 035601 (2021).

[53] The interlayer distance between the monolayers of the transition metal ditellurides is greater in $ZrTe_2$ (3.3 Å) than in $NiTe_2$ (2.59 Å). This is the reason the Fermi surface looks more 3D in $NiTe_2$.

[54] According to Onsager's relation, the quantum oscillation measured frequency of an electron orbit F which is perpendicular to the applied magnetic field is related to the area of the Fermi surface A by $F = \frac{\phi_0}{2\pi^2}A$, where $\phi_0 = 2.07 \times 10^{-15}$ T m^2 is the quantum of flux.

[55] D. Rhodes, R. Schönemann, N. Aryal, Q. Zhou, Q. R. Zhang, E. Kampert, Y.-C. Chiu, Y. Lai, Y. Shimura, G. T. McCandless, J. Y. Chan, D. W. Paley, J. Lee, A. D. Finke, J. P. C. Ruff, S. Das, E. Manousakis, and L. Balicas, Bulk Fermi surface of the Weyl type-II semimetallic candidate γ-$MoTe_2$, Phys. Rev. B **96**, 165134 (2017).